J. Fluid Mech. (1986), *vol.* 172, *pp.* 211–229
Printed in Great Britain

Organized structures in a turbulent plane jet: topology and contribution to momentum and heat transport

By R. A. ANTONIA, A. J. CHAMBERS, D. BRITZ AND L. W. B. BROWNE

Department of Mechanical Engineering, University of Newcastle, N.S.W., 2308, Australia

(Received 27 September 1984 and in revised form 2 April 1986)

In the self-preserving region of a slightly heated turbulent plane jet, conventional isocorrelation contours of velocity and temperature fluctuations support the existence of organized large-scale structures. Temperature fronts associated with these structures were visually detected using a spanwise rake of cold wires. This method of detection was then used to condition velocity and temperature fluctuations and products of these fluctuations. Ensemble-averaged velocity vectors, constructed in the plane of main shear, suggest a topology for the organized motion in which the temperature front is identified with the diverging separatrix connecting adjacent structures on the same side of the centreline. Coherent stresses and heat fluxes are particularly significant near the diverging separatrix. Contributions by the coherent and random motions to the averaged momentum and heat transports are generally of the same order of magnitude.

1. Introduction

In a previous paper (Antonia *et al.* 1983, hereafter referred to as I) the existence of large-scale quasi-organized structures in the fully turbulent far field of a plane jet was established and discussed in the context of supporting evidence obtained by other investigators (e.g. Cervantes de Gortari & Goldschmidt 1981; Oler and Goldschmidt 1981, 1982; Mumford 1982). Oler & Goldschmidt (1981, 1982) suggested that these structures were arranged in a quasi-two-dimensional Kármán-like vortex street with axes aligned in the spanwise direction. Mumford (1982) indicated that the previous roller-like structures co-existed with other structures (e.g. Townsend 1976) aligned in the direction of the principal axis of strain. No specific spatial relationship between these two types of structures has been formulated. Also, flow visualization, while confirming the presence of the roller-like structures (e.g. the smoke-wire visualization of Goldschmidt, Moallemi & Oler 1983), has generally provided little insight into the topology of these structures.

The main aims of the present investigation were to provide information on the topology of the structures and to address the important question of the contribution that these structures make to the momentum and heat transport. We consider only the nearly self preserving region of the flow where the structures, which may be considered as two-dimensional only over a spanwise region of the order of the jet half-width, are asymmetric with respect to the centreline of the jet. Contributions of the structures to the momentum and heat transfer can in principle be determined from conditionally averaged products of velocity and temperature fluctuations. To

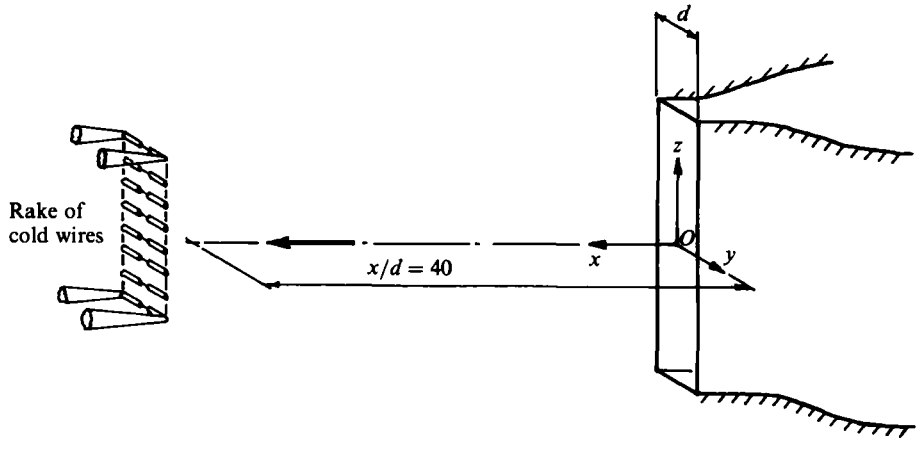

FIGURE 1. Schematic arrangement of plane jet, showing coordinate axes and spanwise rake of cold wires. The scale of the rake is exaggerated.

determine conditional averages accurately, a reliable detection scheme must be used. The advantages of using a scheme based on information obtained at several points in space were noted by Subramanian *et al.* (1982). Accordingly, the detection in the present study was based on information obtained at several points at the same x (streamwise) and y (lateral or main shear) but different z (spanwise) locations in the flow (see figure 1). As in the work of Chem & Blackwelder (1978) and Subramanian *et al.* (1982), use is made of temperature as a passive marker of the flow with the implicit assumption that the spatially coherent temperature fronts are characteristic parts of the structures.

The experimental arrangement is detailed in §2. Before considering conditional statistics, conventional space–time correlation data are discussed in §3 as these data complement and extend the conventional statistics already considered in I. Following a brief description of the multi-point detection scheme in §4, conditional averages obtained with this scheme are presented in §5 and interpreted in terms of the topology of the structures. Contributions by the structures to the average transport of momentum and heat are considered in §6.

2. Experimental arrangement and measurement description

The plane jet facility has been described in I. It is sufficient to mention here that the vertical nozzle has a width $d = 12.7$ mm and an aspect ratio of 20:1. The nozzle was fitted with an end plate (width = 25.5 cm and height = 28 cm) with confining horizontal (x, y)-plane plates (each of width = 0.7 m and length = 1.1 m). The flow was heated to a temperature T_j at the nozzle exit of about 25 °C above ambient when the jet velocity U_j was about 9 m/s. All measurements presented in this paper were made at $x/d = 40$. Profiles of Reynolds normal and shear stresses, heat fluxes and higher-order moments of velocity and temperature fluctuations indicated that self-preservation was approximately satisfied at $x/d > 20$. Profiles of mean velocity aand mean temperature, less sensitive indicators of self-preservation, achieved similarity at a much smaller x/d.

At $x/d = 40$, where all the measurements presented in the following sections were obtained, the centreline mean velocity U_0 was approximately 3.4 m/s and the

centreline mean temperature, with respect to ambient, T_0 was about 9 °C. The mean velocity half-width L_u was about 60 mm. The experimental variations of L_u, U_0 and T_0, for $x/d \gtrsim 20$, were given by $L_u/d = 0.104(x/d+5)$, $(U_j/U_0)^2 = 0.143(x/d+9)$ and $(T_j/T_0)^2 = 0.18(x/d+8)$. Normalization of results is indicated by using an asterisk. Lengths are normalized by L_u, time by L_u/U_0, velocities by U_0 and temperatures by T_0.

For this flow Gr/Re^2 is about 0.0015 [$Gr = gL_u^3(T_0-T_\infty)/\nu^2 T_\infty$, $Re = U_0 L_u/\nu$] thus discounting any buoyancy effect and justifying the use of temperature as a passive contaminant. Results were obtained with primarily three types of measurements:

(*a*) Velocity fluctuations u and v (in the x- and y-directions respectively) and temperature fluctuations θ were measured separately using fixed and movable probes in two experiments. In one experiment the velocity fluctuations were measured using X-wires in the unheated flow. The fixed X-wires were located at $z = 0$, $y = |L_u|$ and the movable X-wires, at the same x and z, were traversed in the y-direction across the jet. The other experiment was carried out in the heated flow with a fixed cold wire located at $z = 0$, $y = |L_u|$ and a movable cold wire traversed in the y-direction across the jet.

(*b*) Temperature fluctuations were measured using a rake of eight cold wires aligned in the spanwise z-direction (figure 1) and evenly distributed on either side of the y-axis; the separation between the extreme wires of the rake being $0.9L_u$. The rake was moved to various y-positions.

(*c*) Fluctuations u, v and θ were measured using an X-probe/cold-wire arrangement in the rake of cold wires. Apart from the cold wire located 0.5 mm upstream of the X-wires, five other cold wires were used in this rake. The X-wires/cold-wire arrangement was located at $z = 0$ while the extreme cold wires were at $z = +0.42L_u$ and $-0.64L_u$. The rake was traversed across the jet to obtain results for a range of y values.

For (*a*) and (*c*), the wires used in the X-probes were 5 μm Pt–10% Rh Wollaston (length ≈ 0.6 mm, separation ≈ 0.6 mm). For (*c*), the X-probe was designed and constructed as an integral part of the rake described by Subramanian *et al.* (1982) with the centre of the X-probe aligned with the cold wires above and below it. All cold wires for (*a*), (*b*) and (*c*) consisted of 0.63 μm Pt–10% Rh Wollaston of approximately 0.6 mm length.

The hot wires were operated with constant-temperature anemometers (DISA 55M10) at an overheat of 0.8. The cold wires were operated in constant-current (0.1 mA) circuits. The signals from hot and cold wires were usually recorded on an eight-channel FM tape recorder after appropriate signal conditioning. These signals were subsequently digitized at a sampling frequency of 5951 Hz using a digital data acquisition system (11 bits+sign A/D converter with sample and hold channels) and a PDP 11/34 digital computer. In a few experiments, the eight hot-wire/cold-wire signals were digitized directly.

The X-wires were calibrated for yaw and velocity while the cold wires were calibrated for temperature sensitivity. These calibrations were carried out with the wires in the nozzle exit plane and use was made of a data logger consisting of a data acquisition system (HP3497A) and a desktop computer (HP85). During calibration, the jet velocity was measured with a Pitot tube and a Furness micromanometer with a least count of 0.01 mm H_2O. The jet mean temperature was measured with a 10 Ω Pt resistance thermometer and a Leeds & Northrop (8078) temperature bridge with a least count of 0.01 °C.

Results in this paper are shown only for a range of $|y^*|$ extending to about 1. It

was found in I that flow reversal, as detected by the cold wire upstream of the X-probe, was first detected at $|y^*| \approx 1$ so that fluctuations u and v are significantly in error at larger $|y^*|$.

3. Space–time correlations of velocity and temperature fluctuations

In I, correlations obtained from velocity and temperature fluctuations at two points, separated in the y-direction but with zero separation in the x- and z-directions, were presented only for zero time delay. This information is presented in this section in the form of correlation contours in a time-delay y or (x, y)-plane. Similar information was presented by Oler & Goldschmidt (1981) and Mumford (1982) for the u-fluctuation only. The present contours extend these correlations to v- and θ-fluctuations.

For measurements of type (a) [see §2], one X-probe was fixed at $y^* = -1$ and the other, at the same x- and z-locations as the first probe, was traversed across the jet up to $y^* = 1$. For temperature measurements, one cold wire was fixed at $y^* = 1$ and the other traversed across the jet to $y^* = -1$. The temperature measurements were taken much later than the velocity measurements and unfortunately the fixed position was not the same as for the velocity measurement. If y_1^* and y_2^* denote the y-locations of the fixed and moving probes respectively, the correlation function (only autocorrelations are considered here) between fluctuations α ($\equiv u$, v, or θ) is defined as $\rho_\alpha(y_1^*, y_2^*; \tau^*) = \overline{\alpha(y_1^*, t^* - \tau^*)\,\alpha(y_2^*, t^*)}/\alpha'(y_1^*)\,\alpha'(y_2^*)$, where the prime denotes an r.m.s. value and t^* and τ^* are the time and time delay respectively. The correlation function was obtained by first applying a standard FFT algorithm on records of typically 2–3 min duration to obtain the cospectrum. An inverse FFT was then applied to this cospectrum to determine the correlation function ρ_α. The time delay τ may be interpreted as a distance Δx (and consequently a change in x/d) via the relation $\Delta x = -U_c \tau$, where U_c is an appropriate convection velocity of the structures. Several estimates of U_c were made in I, using different methods and here we have used the one obtained by determining τ_{max}, the time delay that gave the maximum correlation between v-fluctuations measured with two X-wires, separated in x but located at the same y^* and z^*. The approach yielded a convection velocity $U_c \approx 0.65\,U_0$, approximately independently of $|y^*|$. This convection velocity was used to determine Δx^* and the x/d-values in figure 2(a–c) which shows the contours of constant correlation for u, v and θ respectively.

A comparison of the ρ_u contours in figure 2(a) with those published by Oler & Goldschmidt (1981), see also Goldschmidt *et al.* (1983) and Mumford (1982), suggests points of similarity as well as small quantitative differences. The present contours of ρ_u are similar to the other published data; they change sign at $y^* \approx 0$, i.e. approximately when the traversing probe crosses the centreline of the jet. The tilt obtained, as the observer moves away from the centreline, of both positive and negative contours towards smaller values of x/d is present in Mumford's contours but is not strongly evident in those of Oler & Goldschmidt (1981), perhaps because of slight differences in the location of the fixed probe. The alternating positive–negative pattern of the ρ_u contours support, as noted by Oler & Goldschmidt (1981), the existence of counter-rotating vortices positioned on opposite sides of the centreline and recurring periodically, at least over a sufficiently large streamwise extent. The range of x/d or Δx^* over which the contours in figure 2(a) indicate a correlation is sufficiently large to also support Oler & Goldschmidt's suggestion that, for this flow, there exist coherent structures in the form of a vortex-street pattern. Such a pattern

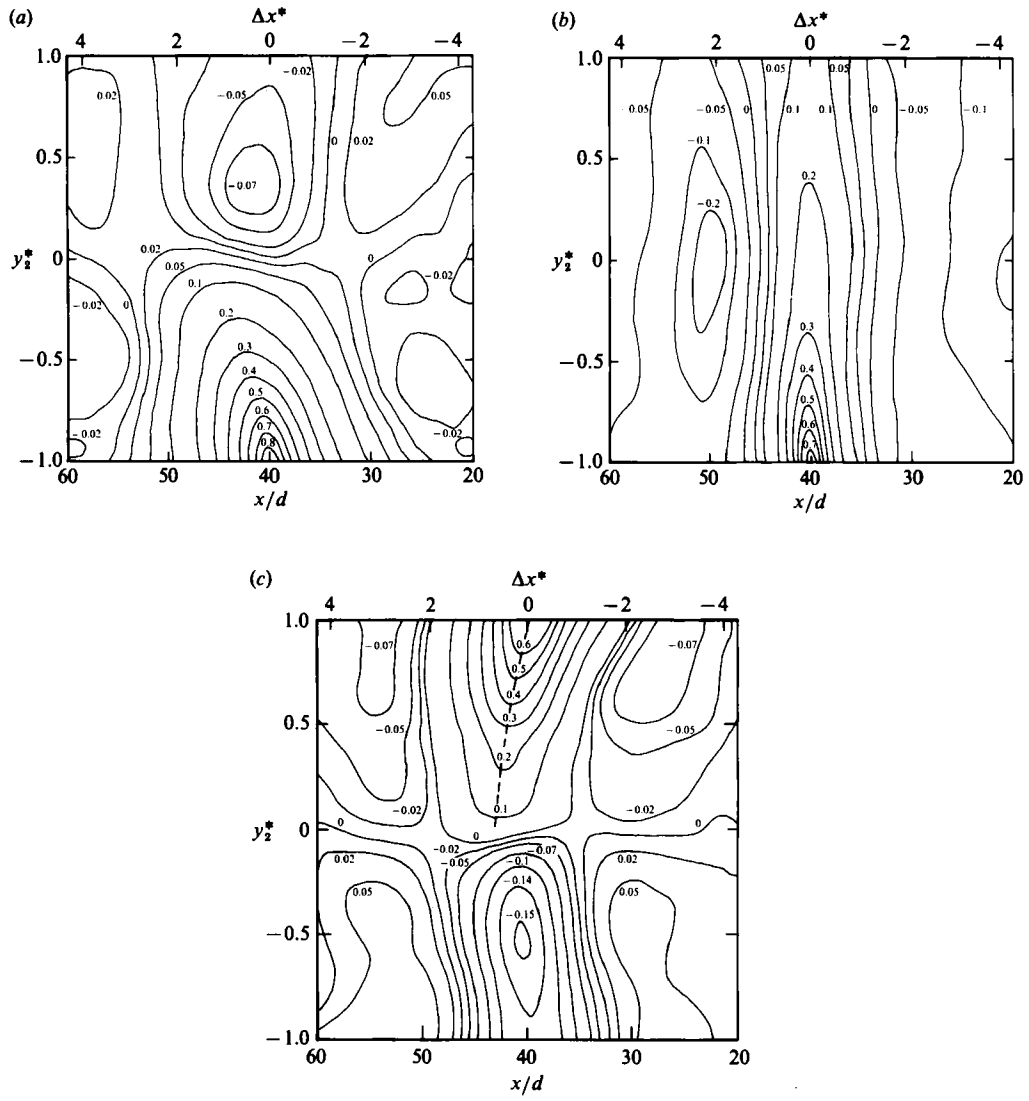

FIGURE 2. Isocorrelation coefficient contours of longitudinal and lateral velocity fluctuations and of temperature fluctuations. (*a*) $\rho_u(y_1^*, y_2^*; \Delta x^*)$; (*b*) $\rho_v(y_1^*, y_2^*; \Delta x^*)$; (*c*) $\rho_\theta(y_1^*, y_2^*; \Delta x^*)$. For (*a*) and (*b*), $y_1^* = -1$. For (*c*), $y_1^* = 1$. The broken curve in (*c*) is the locus of maxima of ρ_θ.

would induce an asymmetry, with respect to the centreline, not only in the velocity fluctuation u but also in the temperature fluctuation θ. Indeed, the ρ_θ contours in figure 2(*c*) do display the same alternating positive–negative pattern exhibited by ρ_u and closely reflect the features exhibited by the ρ-contours. This similarity follows from the analogous boundary conditions for u and θ and supports the use of temperature as an effective passive marker of the flow. For the proposed counter-rotating vortex-street pattern, correlations between v-fluctuations should not change sign with y but one could speculate that the ρ_v pattern would change sign periodically in the x-direction. This speculation is confirmed by the contours of figure 2(*b*) which stretch across the jet centreline and are generally narrower with respect to x than ρ_u or ρ_θ. The streamwise distance between the locations of the maximum and

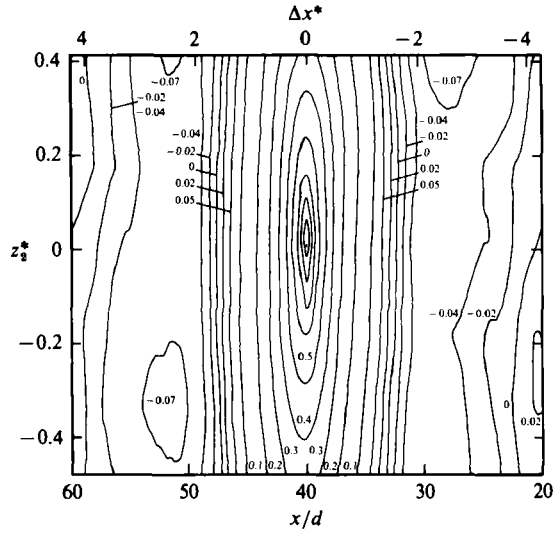

FIGURE 3. Isocorrelation coefficient contours of temperature fluctuations obtained with a spanwise rake of cold wires located at $y^* = 1$. Correlations are relative to the wire at $z_1^* = 0$.

minimum values of ρ_α in figure 2 is about $11d$ ($\approx 2.3L_u$), representing a rough estimate of the streamwise extent of the structures. The distance between locations of successive minima of ρ_α is about $23d$ ($\approx 4.8L_u$), representing a rough estimate of the streamwise wavelength of the structures.

Temperature isocorrelation contours in the (x, z)-plane were determined from the temperature signals obtained with the spanwise rake [measurements of type (*b*), §2]. In the context of the previous definition of ρ_α for measurements in the (x, y)-plane, ρ_θ is now understood to represent $\rho_\theta(z_1^*, z_2^*; \Delta x^*)$ with the fixed probe at the centre, $z_1^* \approx 0$, of the rake. The location z_2^* of the 'moving' probe is taken to be that of any other probe in the rake. Only contours obtained with the rake at $y^* = 1$ are shown in figure 3 but contours determined at several other values of y^* in the range $0 \leqslant y^* \leqslant 1$ are almost identical with those shown in the figure. For the present range of z^*, the maximum value of ρ_θ always occurred at $\Delta x^* = 0$. A similar result was obtained for the spanwise u-autocorrelation in a plane jet presented by Moum, Kawall & Keffer (1979) but, in their case, the magnitude of ρ_u at corresponding values of z_2^* is smaller than the present value of ρ_θ. Thus the spatial coherence of the flow structure is almost as large in the (x, z)-plane as in the (x, y)-plane, although note that this result is based only on conventional (long-time averaged) correlations. Short-time correlations were not calculated and a definite statement cannot be made on the relative extents of the coherent structures in the (x, y)- and (x, z)-planes. Contours in the (x, z)-plane of instantaneous temperature fluctuations suggested however that the extent of the structure could be significantly larger than the z-range used for viewing the structures or that implied by the long-time averaged contours of figure 3. In the (x, y)-plane one would expect the extent of the structures to be limited by the presence of the turbulent/non-turbulent interface and the flow centreline. It would therefore be reasonable to expect the structures to extend further in the (x, z)-plane than in the (x, y)-plane. Further support for the relatively strong coherence in the spanwise direction is provided by the spectral coherence (defined in the usual manner, e.g. Bendat & Piersol 1966) between temperature fluctua-

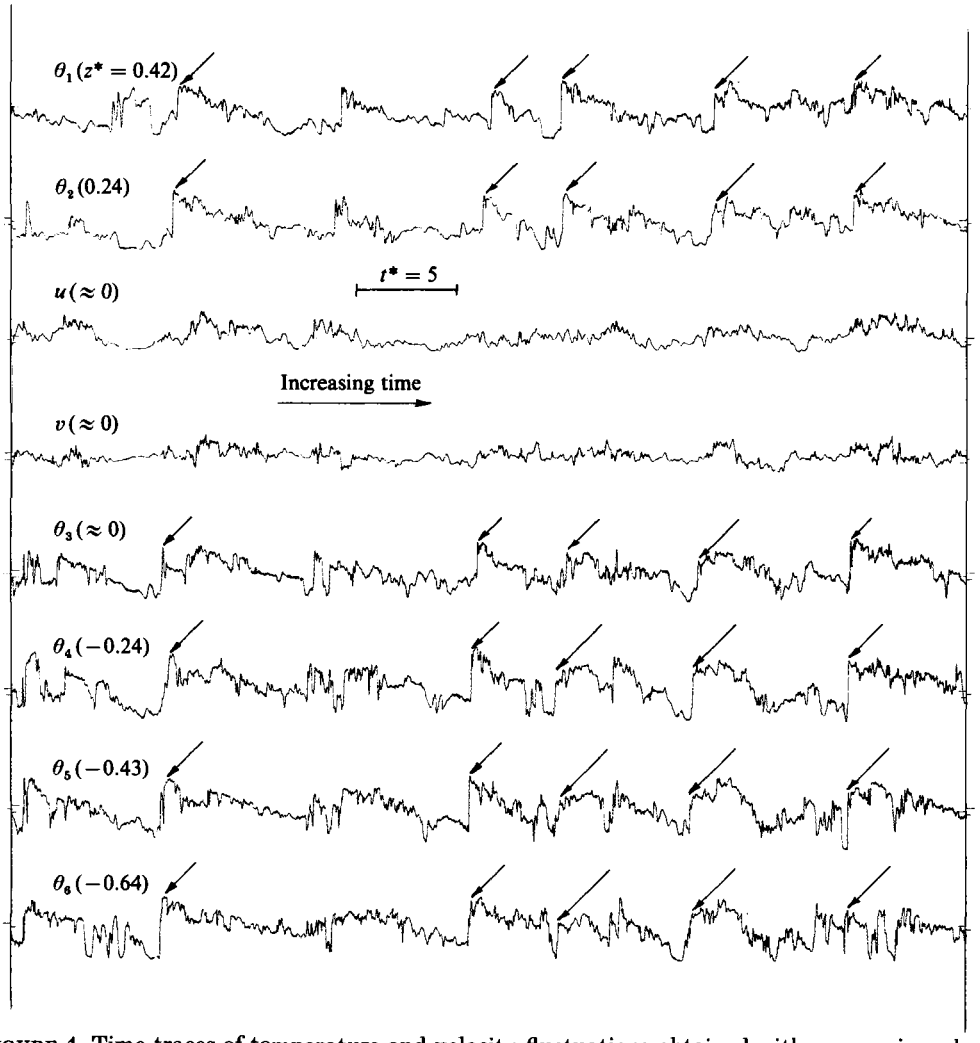

FIGURE 4. Time traces of temperature and velocity fluctuations obtained with a spanwise rake of cold wires at $y^* = 1$. Arrows point to temperature fronts identified by eye.

tions at z_1^* and z_2^*. The calculated maximum value of this coherence was as large as 0.4 at $z_2^* = \pm 0.5$ and always occurred at a non-dimensional frequency f^* $(\equiv fL_u/U_0) \approx 0.11$, in numerical agreement with the average frequency of the structures determined by different methods in I and Cervantes & Goldschmidt (1981).

4. Detection of the structure for conditional averaging

To determine reasonably accurately conditional averages it is important that a reliable detection scheme be used. Chen & Blackwelder (1978) and Subramanian *et al.* (1982) detected temperature fronts in a turbulent boundary layer with a rake of cold wires aligned in the y- or main-shear direction. Chambers *et al.* (1983) suggested that the detection of fronts in a boundary layer could be made less ambiguously with a rake aligned in the z-(spanwise) direction than with a rake aligned in the y-direction. This suggestion was followed here. An example of the temperature traces obtained with the rake at $y^* = 1$ is given in figure 4. At this location, the flow begins to be

intermittent; the turbulent/non-turbulent intermittency factor determined from the probability density function of temperature is about 0.92 at $y^* = 1$, in reasonable agreement with the value of 0.95 measured by Jenkins & Goldschmidt (1976) at a corresponding location in a plane jet. The temperature fronts, identified with arrows, are characterized by a relatively sudden increase in temperature and occur, on average, with almost no time delay at all locations of the rake. There is evidence however that individual fronts can be slightly inclined in the (x, z)-plane. By examining several hundred fronts, curved fronts were identified by a later arrival time at the edges than near the centre of the rake. These inclined and curved fronts are not inconsistent with the conventional contours of figure 3 which indicate that, on average, the maximum spanwise correlation occurs at zero time delay. The range of z^* covered by the rake is larger by about 50% than the estimate (≈ 0.7, given in I), based on long-time-averaged correlations, for the spanwise extent of the motion. Temperature jumps that occur in several successive traces but which could not be detected on all traces have not been counted as fronts. This criterion may appear to be unnecessarily strict and therefore biased, but it was deliberately retained in an effort to focus only on 'clean' structures, i.e. those that are unsmeared due, for example, to the interaction with neighbouring structures. Some *a posteriori* justification for this decision is given in §6.

A comparison was made by Antonia *et al.* (1984) between the present visual detection procedure and a scheme such as VITA (variable interval time averaging, Blackwelder & Kaplan 1976) which is based on information obtained at only one point in space. The comparison indicated that more reliable conditional averages could be obtained with the visual procedure. Chambers *et al.* (1983) suggested an extension of VITA to a multipoint procedure. Although this procedure appears promising, we have, for the present work, preferred the visual detection combined with a single-point VITA.

A visual scrutiny of the computer-plotted traces of the six cold wires allowed a rough estimate to be made of the instants at which temperature fronts occurred. VITA was then applied to the temperature signal at the X-wire location (θ_3 in figure 4) and only those VITA detections that agreed to within ± 15 data points with the visually detected fronts were accepted. VITA was used with a small value of the threshold parameter (details are given in Antonia *et al.* 1984) to maximize the number of VITA detections and therefore their coincidence with visual detections. A coincidence of about 85% was typical, independent of y^*. All the fronts indicated in figure 4 were accepted by the above approach.

5. Conditional averages

A conditional average is defined as follows. Consider N equispaced values of an experimentally obtained time series of a quantity β, defined by β_j, $j = 1, \ldots, N$, for which a detection of structures criterion has resulted in n detections. Let i be the value of j at any particular detection (there will be n values of i) and let k be the distance from i, in number of data points, at which a conditional average is required. Then the conditional average of β at k is defined by

$$\langle \beta \rangle_k = \frac{1}{n} \sum_{\text{all } i} \beta_{i+k}. \tag{1}$$

If a 'window' of $2l+1$ points is selected to cover the range over which conditional averages are required then k will vary from $-l$ to $+l$. In our work N was 320000,

n varied between 120 and 150 and l was 400. The window size was approximately the average wavelength of a coherent structure.

To provide a framework for discussion of the measured conditional averages, we have used a triple decomposition although, as pointed out by Cantwell & Coles (1983) and Hussain (1983), the assumption that the coherent structure is a perturbation of the mean flow may be an oversimplification. Consider, for example, the x-direction velocity fluctuation at a single point $i+k$. We can write

$$u_{i+k} = \langle u \rangle_k + u_{\mathrm{r},\, i+k},$$

where u_{r} is identified as the random or incoherent fluctuation at that point. The instantaneous velocity at this point will be

$$U_{i+k} = \overline{U} + u_{i+k},$$

where the overbar denotes a conventional average. Thus we get the triple decompositions

$$\left.\begin{aligned} U_{i+k} &= \overline{U} + \langle u \rangle_k + u_{\mathrm{r},\, i+k} \\ V_{i+k} &= \overline{V} + \langle v \rangle_k + v_{\mathrm{r},\, i+k} \\ T_{i+k} &= \overline{T} + \langle \theta \rangle_k + \theta_{\mathrm{r},\, i+k} \end{aligned}\right\}. \tag{2}$$

Note that $\langle u_{\mathrm{r}} \rangle_k$, $\langle v_{\mathrm{r}} \rangle_k$ and $\langle \theta_{\mathrm{r}} \rangle_k$ will, by definition, be zero. Conditional averages of products can be written as

$$\begin{aligned} \langle uv \rangle_k &= \frac{1}{n} \sum_{\text{all } i} u_{i+k} v_{i+k} \\ &= \frac{1}{n} \sum_{\text{all } i} (\langle u \rangle_k + u_{\mathrm{r},\, i+k})(\langle v \rangle_k + v_{\mathrm{r},\, i+k}). \end{aligned}$$

After multiplying and summing, and noting from above that the terms involving $\langle u_{\mathrm{r}} \rangle$ and $\langle v_{\mathrm{r}} \rangle$ will be zero, we get

$$\left.\begin{aligned} \langle uv \rangle_k &= \langle u \rangle_k \langle v \rangle_k + \langle u_{\mathrm{r}} v_{\mathrm{r}} \rangle_k. \\ \text{Similarly} \quad \langle u\theta \rangle_k &= \langle u \rangle_k \langle \theta \rangle_k + \langle u_{\mathrm{r}} \theta_{\mathrm{r}} \rangle_k \\ \langle v\theta \rangle_k &= \langle v \rangle_k \langle \theta \rangle_k + \langle v_{\mathrm{r}} \theta_{\mathrm{r}} \rangle_k. \end{aligned}\right\} \tag{3}$$

Using the detection scheme described in §4, conditional averages of u, v, θ and their products were computed using (1), from records of approximately 60 s duration, at several values of y^* and the results are shown in figure 5. In this figure positive τ_1^* indicates a time after the front is detected, and the location $\tau_1^* = 0$ was arbitrarily the same for all values of y^*. For clarity of presentation, the conditional averages shown in figure 5 are for only four values of y^* and some soothing was applied to the computer-plotted averages. The magnitudes of the averages have been normalized by U_0 and/or T_0. Although conditional measurements were obtained at only one value of x/d, the normalization in figure 5 is such that the averages should approximately satisfy self-preservation.

Conditional averages in figure 5 indicate an increase in $\langle \theta^* \rangle$ near $\tau_1^* = 0$, which is accentuated by comparison with $\langle u^* \rangle$ or $\langle v^* \rangle$. The use, in the detection, of either u or v instead of θ would have resulted (e.g. Subramanian *et al.* 1982) in a sharpening of $\langle u^* \rangle$ or $\langle v^* \rangle$ but would not qualitatively affect the comparison. Observations of the u-, v- and θ-signals in figure 4 show that, at the fronts, the gradients in θ are larger than those in u or v.

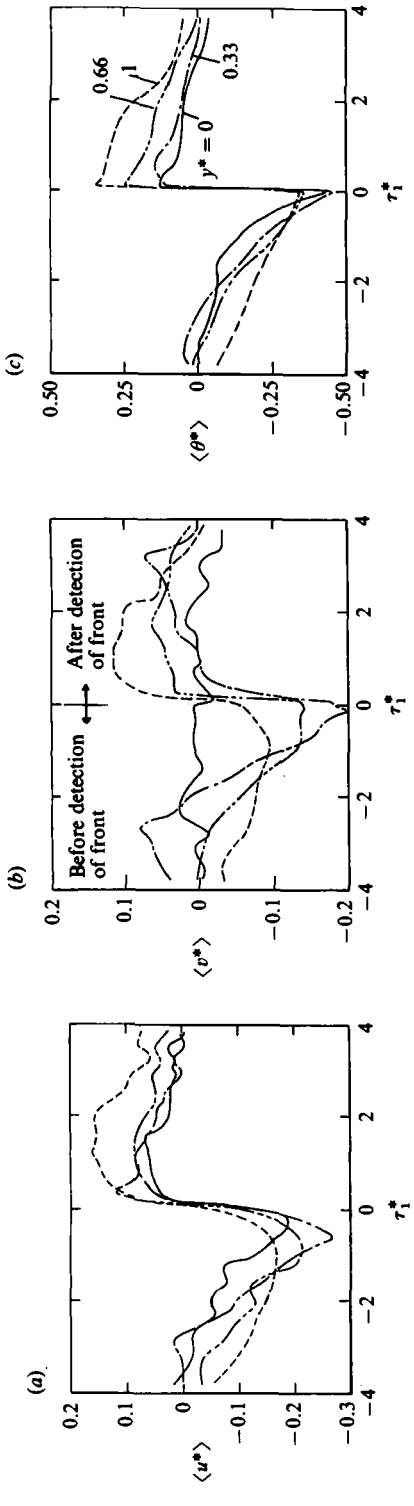

FIGURE 5. Conditional averages of u, v, θ, and their products obtained at four values of y^*. (*a*) $\langle u^* \rangle$; (*b*) $\langle v^* \rangle$; (*c*) $\langle \theta^* \rangle$; (*d*) $\langle u^* v^* \rangle$; (*e*) $\langle u^* \theta^* \rangle$; (*f*) $\langle v^* \theta^* \rangle$: ——, $y^* = 0$; – – –, 0.33; — – — –, 0.66; — — —, 1.

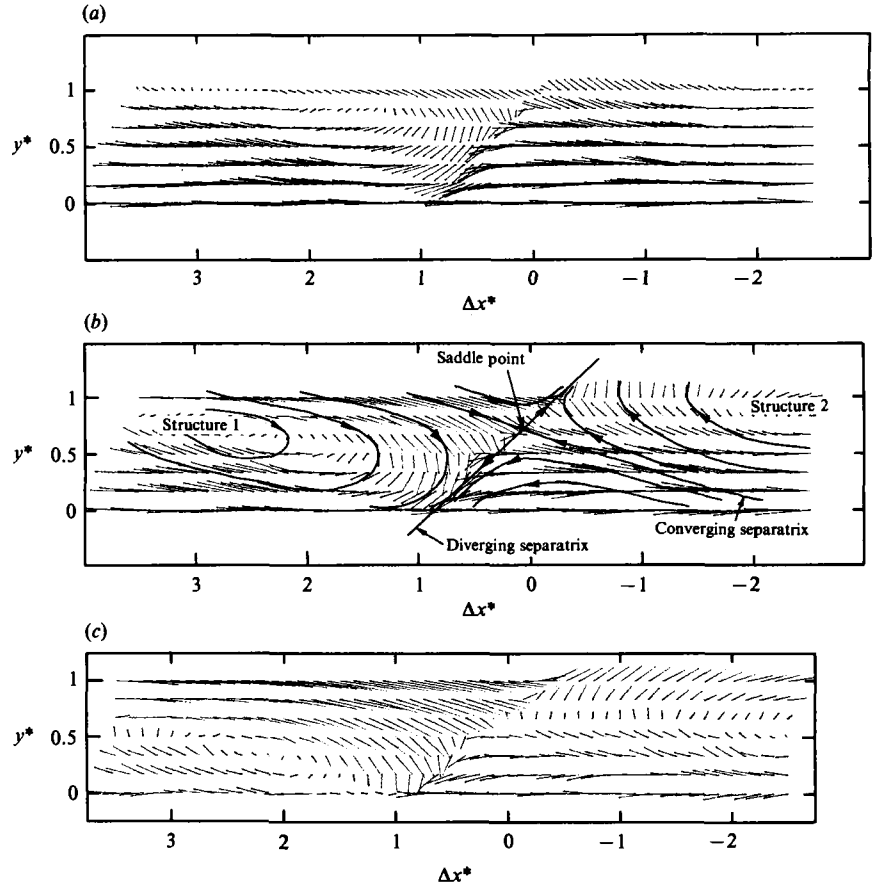

FIGURE 6. Conditional-averaged velocity vectors relative to an observer travelling at a velocity of U_c, the assumed convection velocity of the structures. Note $\Delta x^* = 0$ is the instant of detection of the temperature front at $y^* = 1$. (*a*) $U_c = 0.5\,U_0$; (*b*) $0.65\,U_0$; (*c*) $0.8\,U_0$.

Conditional averages at the larger values of y^* are characterized by significant positive values of all three quantities and of their products for positive values of τ_1^*, i.e. after the front is detected. Closer to the jet axis, and for negative values of τ_1^*, $\langle u^* \rangle$, $\langle v^* \rangle$ and $\langle \theta^* \rangle$ have large negative values. This trend is accompanied by correspondingly large positive values in the conditional averages of the products. At $y^* = 0$, there is no significant variation in $\langle v^* \rangle$ and this is consistent with the requirement of symmetry at the centreline. However, at this point, there are significant increases near $\tau_1^* = 0$ in $\langle u^* \rangle$ and $\langle \theta^* \rangle$. Correspondingly, the product $\langle u^* \theta^* \rangle$ is significant at $y^* = 0$ and this is consistent with the non-zero magnitude of $\overline{u\theta}$ at this location. Not surprisingly, the changes in $\langle v^* \theta^* \rangle$ and especially $\langle u^* v^* \rangle$ are small near $\tau_1^* = 0$, these products tending to fluctuate about zero. The general behaviour of $\langle u^* \rangle$, $\langle v^* \rangle$ and $\langle \theta^* \rangle$ is consistent with the lateral distributions of the conventional skewness S_α ($\equiv \overline{\alpha^3}/\alpha'^3$) of the fluctuations u, v and θ. For example at $y^* = 0$, the measured skewness of v is zero while $S_\theta \approx -0.7$. At $y^* = 1$, $S_\theta \approx 0$ and the conditional average of θ^* is nearly antisymmetrical with respect to $\tau_1^* = 0$.

A physical interpretation of the results in figure 5 is best obtained after the $\langle u^* \rangle$ and $\langle v^* \rangle$ distributions are used to construct (figure 6) a streamline pattern for the large-scale motion. Whereas in figure 5, the location $\tau_1^* = 0$ was arbitrarily the same

for all values of y^*, in figure 6, it was necessary to correct for the inclined front by initially having $\Delta x^* = 0$ (as before $\Delta x = -U_c \tau_1$) correspond to the time at which the temperature front is detected at $y^* = 1$. Conditional averages at smaller values of y^* were then positioned by shifting Δx^*, at each value of y^*, by an amount corresponding to that at which the temperature correlation (figure 2*c*) is maximum. The locus of these points is shown as a dashed line in figure 2(*c*). The results for three different convection velocities U_c are displayed in a frame of reference moving at a velocity U_c. Consequently, the length of each velocity vector in figure 6 is $[(\overline{U}+\langle u\rangle - U_c)^2 + (\overline{V}+\langle v\rangle)^2]^{\frac{1}{2}}$ and its direction is $\tan^{-1}[(\overline{U}+\langle u\rangle - U_c)/(\overline{V}+\langle v\rangle)]$. This construction is similar to that used by Thomas & Brown (1977) in a turbulent boundary layer. $\overline{U}$ was determined for each y from a self-preserving form of the velocity profile and $\overline{V}$ was calculated for each y from the continuity equation. The maximum value of $\overline{V}^*$ is about 0.016 at $y^* \approx 0.6$ so that $\overline{V}$ is significantly smaller than $\overline{U}$ and its inclusion in the calculation of the velocity vector is strictly unnecessary. To avoid confusion, vectors in figure 6 are shown for every sixteenth point in the time series. The definition of Δx^* is such that the flow direction is always from right to left in the figures. Solid lines in figure 6(*b*) are not calculated streamlines but serve as visual approximations to streamlines and are a useful guide for further discussion.

The conditional-averaged velocity field of figure 6 is referenced to an observer who travels with the convection velocity so the temperature front may be identified with the diverging separatrix connecting adjacent vortical structures. The inclination of the separatrix to the jet centreline was estimated, for $U_c = 0.65\,U_0$, to be about 42°. This estimate is close to that ($\approx 39°$) found for the direction, $0.5\tan^{-1}[\frac{1}{2}(\partial\overline{u}/\partial y)/(\partial\overline{U}/\partial x)]$, for the principal rate of strain. Assuming self-preservation for the mean velocity field, the direction of the principal rate of strain was found to be independent of y^* over the range $0.2 \lesssim y^* \leqslant 0.9$. As can be seen from figure 6(*a* and *c*), U_c values of $0.5\,U_0$ and $0.8\,U_0$, different to the $0.65\,U_0$ obtained using the maximum correlation approach (see §3), do not affect significantly the slope of the separatrix. For $U_c = 0.65\,U_0$ the location of the saddle point, or intersection of the converging and diverging separatrices, is at $y^* \approx 0.75$.

The vector pattern in figure 6(*b*) suggests that a maximum for the coherent vorticity will occur at $\Delta x^* \approx 2.5$ and $y^* \approx 0.7$, the approximate centre of structure 1 (which is more fully delineated than structure 2). The picture tends to become blurred at larger positive or negative values of Δx^* because of the degradation in the conditional averages as $|\Delta x^*|$ increases from the detection instant. Note that there is no attempt, when forming conditional averages with (1), to discriminate between different types of structure, characterized, for example, by different durations or amplitudes of the temperature signatures. The range of Δx^* in figure 6 is sufficiently large to capture slightly more than one average wavelength ($\Delta x^* = 4.9$; close to the estimate in §3) of the structures in the streamwise direction.

Many of the features displayed in figure 5 may now be more effectively interpreted in the light of the flow patterns in figure 6. For example, at larger y^* the positive values (figure 5) of $\langle u^*\rangle$, $\langle v^*\rangle$ and $\langle\theta^*\rangle$ for positive τ_1^* (remember that τ_1^* and Δx^* have opposite signs) reflect the arrival of warmer, higher-velocity fluid from smaller values of y^*. Similarly, at negative τ_1^*, the negative signs of $\langle u^*\rangle$, $\langle v^*\rangle$ and $\langle\theta^*\rangle$ indicate the arrival of cooler, lower-velocity fluid induced towards the jet axis by the downstream vortical structure. Conditional-averaged velocity vectors were also obtained from information obtained at negative values of y^*. The emerging pattern also shows a temperature front aligned with the diverging separatrix connecting

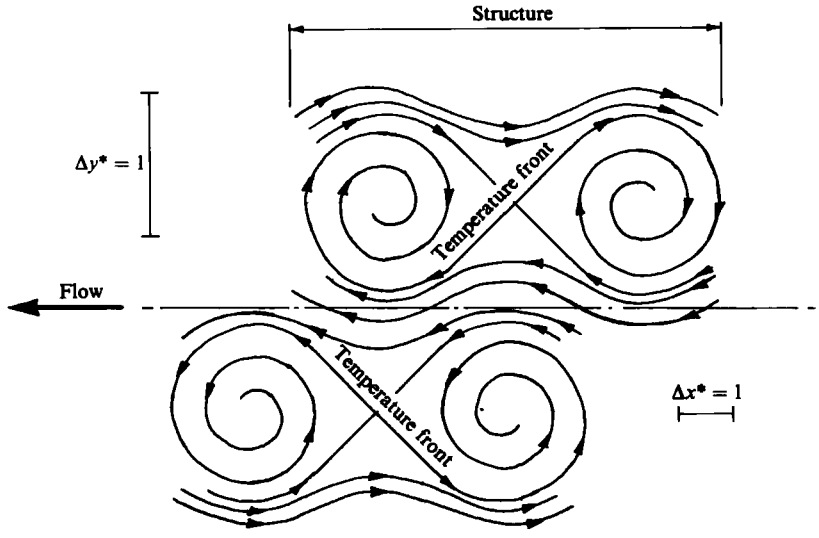

FIGURE 7. Schematic flow topology relative to an observer travelling with the velocity of the centres of the structures.

adjacent vortical structures. The structure downstream of the separatrix has vorticity of opposite sign to that of the corresponding structure at positive y^*. The velocity vectors obtained at negative y^* have not been included in figure 6 as we lack reliable information for unambiguously positioning, in this figure, the front at negative y^* with respect to the front at positive y^*. However, the flow topology, for both positive and negative y^*, that seems consistent with all our results is shown schematically in figure 7. In particular, the flow pattern suggested by figure 7 is consistent with the maintenance of a relatively strong positive v-correlation across the full width of the jet. Also, the entrainment associated with adjacent vortical structures, of either colder ambient fluid or warmer fluid near the jet centreline helps to explain the formation of the temperature fronts on either side of the centreline. The topology of figure 7 differs from that obtained (Cantwell & Coles 1983) in the near field of a wake. It is similar however to the vortex-street pattern observed in the smoke photographs of Perry, Chang & Lim (1982) for a jet issuing from a sinusoidally oscillated rectangular tube with a small Reynolds number (≈ 90). Although the photograph only covered the near field of the jet, the asymmetric disposition of the vortical spanwise structures for our jet was noted in I to first occur in this region. From the information presented in I, we expect that the topology of figure 7 will first be observed in the interaction region of the jet.

Large instantaneous temperature and velocity gradients occur at the temperature front, so that the region near the diverging separatrix should be associated with high turbulent-energy dissipation and temperature dissipation. That this is so can be indirectly inferred from figure 8, which shows the crowding of the coherent production terms for the turbulent energy and lateral heat flux along the general position of the separatrix. Similarly contours of $\langle(\partial\theta/\partial x)^2\rangle$ and $\langle(\partial\theta/\partial z)^2\rangle$, not shown here, exhibit a large concentration around the diverging separatrix.

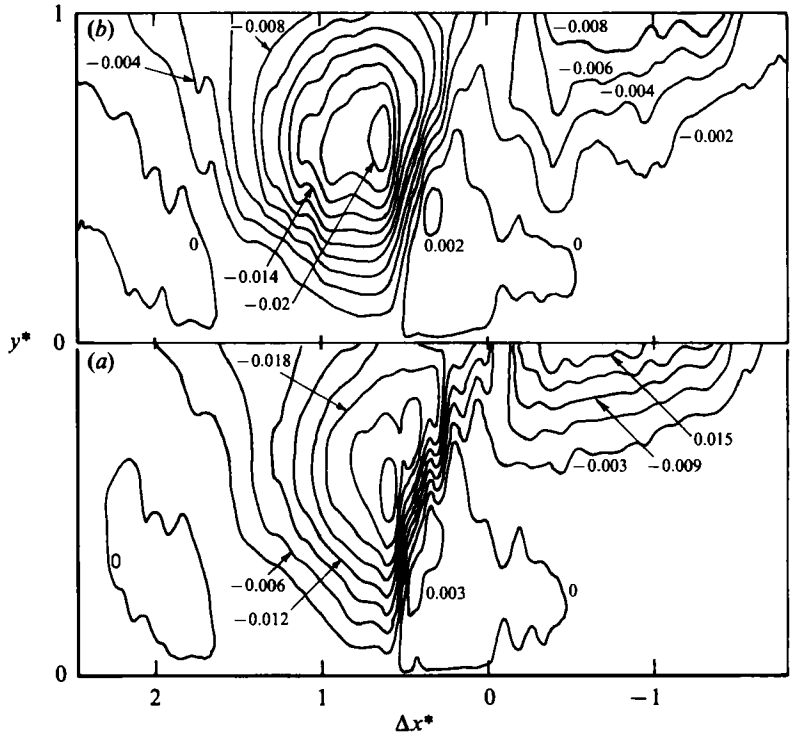

FIGURE 8. Contours of coherent production terms for the turbulent energy and lateral heat flux. (*a*) $\langle u^* \rangle \langle v^* \rangle (\partial \overline{U}^*/\partial y^*)$; (*b*) $\langle v^* \rangle \langle \theta^* \rangle (\partial \overline{T}^*/\partial y^*)$.

6. Contributions of structures to momentum and heat transport

Transport equations for $\overline{U}$, $\langle u \rangle$ and u_r and for the corresponding velocities in the y- and z-directions have been written by Hussain (1983). There are several momentum-transport terms that appear in these equations. For example, the transport equation for U includes gradients, with respect to y, of $\overline{\langle u \rangle \langle v \rangle}$ and $\overline{u_r v_r}$. In addition to the latter two terms, gradients with respect to y of $\langle u \rangle \langle v \rangle$ and $\langle u_r v_r \rangle$ also appear in the transport equation for $\langle u \rangle$. It is not intended to consider here the terms in these equations but it is of interest to consider how terms such as $\langle u \rangle \langle v \rangle$ and $\langle u_r v_r \rangle$ are distributed in the (x, y)-plane.

Contours of constant values of conditional-averaged coherent shear stress and longitudinal and lateral heat-transfer rates are shown in figure 9. The separatrices indicated in figure 6(*b*) have been added to this figure to provide a reference to the flow patterns associated with the structures. All contours are crowded in a region near the separatrix, and maxima in $\langle u^* \rangle \langle v^* \rangle$, $\langle v^* \rangle \langle \theta^* \rangle$ and $\langle u^* \rangle \langle \theta^* \rangle$ occur in this region. There is close similarity between the contours of $\langle u^* \rangle \langle v^* \rangle$ and those of $\langle v^* \rangle \langle \theta^* \rangle$, their extrema occurring at approximately the same coordinates ($\Delta x^* \approx 0.7, y^* \approx 0.5$). This similarily extend to the 'coherent' production terms (not shown here) $\langle u^* \rangle \langle v^* \rangle \partial \overline{U}^*/\partial y^*$ and $\langle v^* \rangle \langle \theta^* \rangle \partial \overline{T}^*/\partial y^*$ for the turbulent energy and temperature variance respectively. All coherent fluxes exhibit large gradients, with respect to both x and y, near the separatrix. Consistently with figure 9, contours of coherent normal stresses $\langle u \rangle^2$, $\langle v \rangle^2$ and coherent temperature intensity $\langle \theta \rangle^2$ were found to have large concentrations where the coherent shear stresses and heat fluxes are largest.

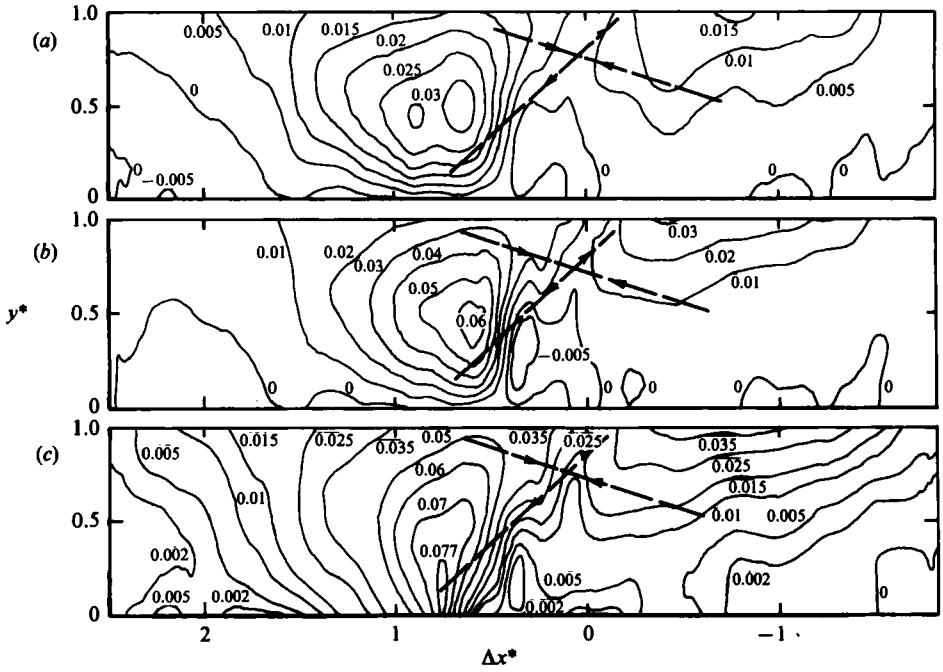

FIGURE 9. Contours of constant values of conditional-averaged coherent shear stress and lateral and longitudinal heat fluxes. (*a*) $\langle u^* \rangle \langle v^* \rangle$; (*b*) $\langle v^* \rangle \langle \theta^* \rangle$; (*c*) $\langle u^* \rangle \langle \theta^* \rangle$.

Contours (figure 10) of the incoherent shear stress and heat fluxes do not have large values where the corresponding coherent quantities are large. The larger values of incoherent fluxes appear to be more uniformly distributed in the (x, y)-plane. The magnitudes of the contours in figure 10 are however unmistakably smaller than those in figure 9.

Antonia *et al.* (1982) and Rajagopalan & Antonia (1981) have estimated contributions from conditionally averaged fluxes in a turbulent boundary layer and a turbulent mixing layer respectively. The same procedure is adopted here, the contributions from the coherent and the incoherent (random) motion to the fluxes being integrated over approximately one wavelength of the structures (801 data points). Denoting this averaging by a tilde, we used

$$\widetilde{\langle \alpha^* \beta^* \rangle} = (\Delta x_2^* - \Delta x_1^*)^{-1} \int_{\Delta x_1^*}^{\Delta x_2^*} \langle \alpha^* \beta^* \rangle \, \mathrm{d}(\Delta x^*),$$

where α, β stand for either $\langle u \rangle$, $\langle v \rangle$, $\langle \theta \rangle$ or u_r, v_r, θ_r. The limits of integration were chosen to be equidistant ($\Delta x_2^* = 2.45$, $\Delta x_1^* = -2.45$) from the location of the front at any value of y^*.

The results, expressed as ratios of the normal averages of the same products, $\overline{\alpha^* \beta^*}$, are shown in figures 11 and 12. The sums of the coherent and incoherent values are also shown and indicate that, within experimental scatter, the coherent values account for all of the contributions. This is an important result and in view of our experimental procedure requires further comment. As noted earlier our detection criteria were set deliberately to be strict to try to ensure that any detections were of a structure that was 'clean', i.e. not smeared in the sense of having an ill-defined form. This resulted in only about 34 % of the total number of data points being used

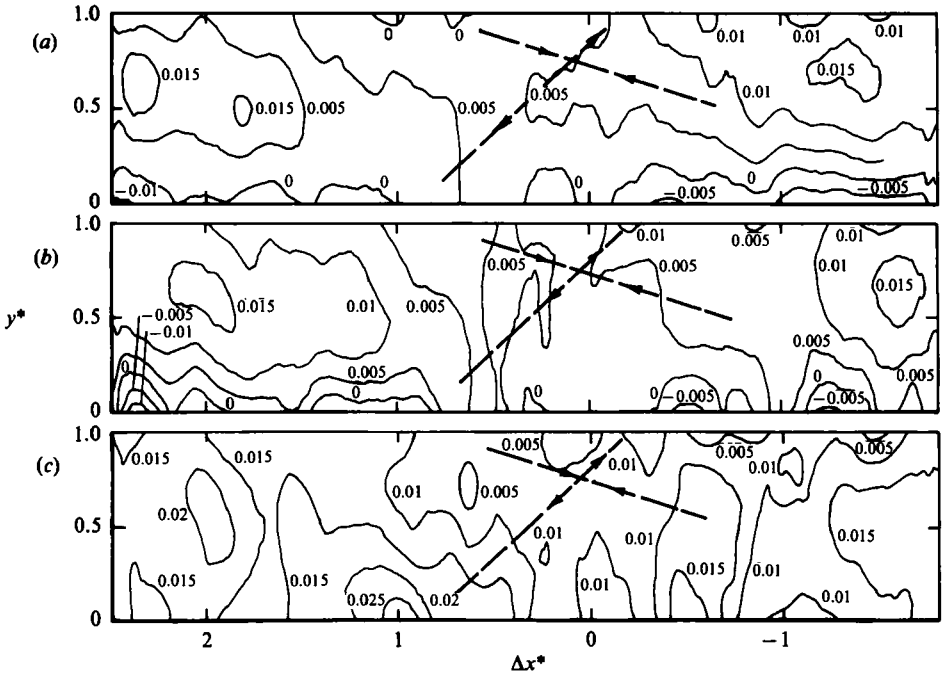

FIGURE 10. Contours of conditional-averaged incoherent shear stress and lateral and longitudinal heat fluxes. (a) $\langle u_r^* v_r^* \rangle$; (b) $\langle v_r^* \theta_r^* \rangle$; (c) $\langle u_r^* \theta_r^* \rangle$.

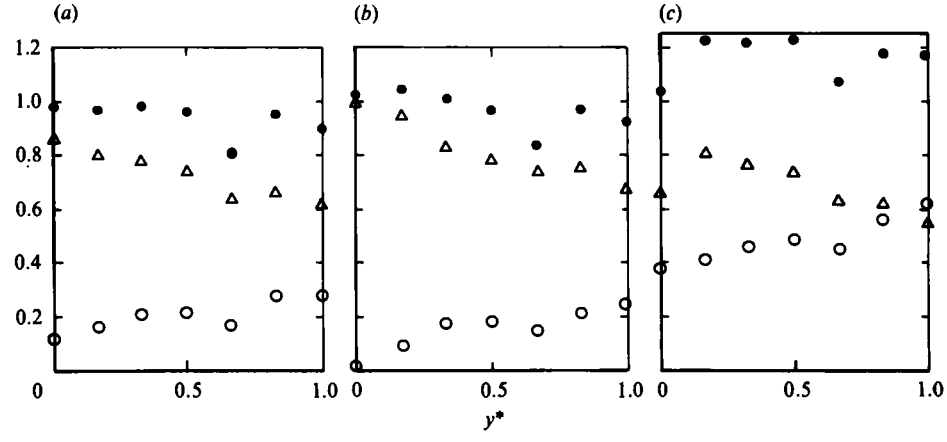

FIGURE 11. Contributions, averaged over one structure, from coherent and incoherent motions to normal stresses and temperature variance: ○, $\widetilde{\langle \alpha^{*2} \rangle}/\overline{\alpha^{*2}}$; △, $\widetilde{\langle \alpha_r^{*2} \rangle}/\overline{\alpha_r^{*2}}$; ●, sum of ○ and △. (a) $\alpha = u$; (b) v; (c) θ.

to establish the above coherent and incoherent averages [i.e. $n(2l+1)/N \approx 0.34$]. It is not difficult to show that

$$1 - \frac{\widetilde{\langle u \rangle \langle v \rangle}}{\overline{uv}} = \left(1 - \frac{N}{n(2l+1)}\right)\left(1 - \frac{\overline{\overline{uv}}}{\overline{uv}}\right),$$

where $\overline{\overline{uv}}$ is the average of uv over the data not included in determining the coherent and random values. Since the left-hand side of this equation is approximately zero,

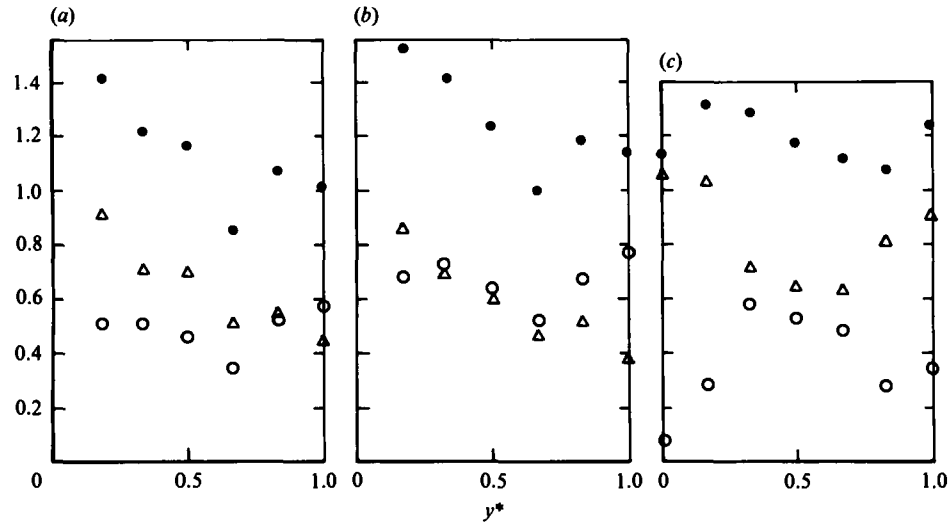

FIGURE 12. Contributions, averaged over one structure, from coherent and incoherent motions to shear stress, lateral and longitudinal heat fluxes: ○, $\langle\widehat{\alpha^*\beta^*}\rangle/\overline{\alpha^*\beta^*}$; △, $\langle\widehat{\alpha_r^*\beta_r^*}\rangle/\overline{\alpha^*\beta^*}$; ●, sum of ○ and △. (*a*) $\alpha = u$, $\beta = v$; (*b*) v, θ; (*c*) u, θ.

we conclude that $\overline{\overline{uv}} \approx \overline{uv}$. This implies that the structures must be space filling in the sense that there can be no significant 'inter-structure' region.

Contributions by the random normal stresses, $\langle u_r^{*2}\rangle$ and $\langle v_r^{*2}\rangle$, figure 11, are much higher, by factors of 3 to 5 than those of the coherent normal stresses. The shear stresses, figure 12, on the other hand tend to be equally distributed between the coherent and random. Temperature variance and heat fluxes also tend to be equally distributed. It is interesting to note that the coherent-contribution ratios tend to be constant across the jet while the random-contribution ratios decrease in all cases, except $u\theta$, as we move out from the jet centreline.

7. Concluding discussion

Isocorrelation contours given in §3 for velocity and temperature fluctuations complement and support the evidence presented in I for organized structures in the nearly self-preserving region of a turbulent plane jet. The subsequent main contributions of the present paper have been to obtain a topological picture of these structures and to estimate their contributions to momentum and heat transport. This was achieved by first identifying sharp changes in temperature over a spanwise distance of the order of the jet half-width and then conditioning the velocity field with respect to this identification.

The topological picture that emerges from the conditionally averaged velocity vectors is that of adjacent vortical structures connected by a diverging separatrix. The temperature front in the present investigation is aligned with the diverging separatrix: this seems plausible when the front is identified with the boundary demarcating the relatively colder fluid entrained or induced by the downstream coherent structure and the warmer fluid induced by the upstream coherent structure. The direction of the temperature front is also close to that of the principal axis of strain. Rajagopalan & Antonia (1981) identified the temperature front in the

turbulent mixing layer of a plane jet with the braid connecting adjacent structures. We believe this diverging separatrix to be dynamically important since it can be identified with a 'shear layer' associated with which are large velocity and temperature gradients. Chen & Blackwelder (1978) put forward a similar idea in connection with a boundary layer, further suggesting that the temperature front provides a dynamical link between the wall and outer regions of the flow. Coherent stresses and heat fluxes are large near this separatrix while the momentum and heat fluxes associated with the incoherent or random turbulence tend to be more uniformly distributed in space. The average contributions from the coherent and incoherent motions are generally of the same order of magnitude, with one exception. The incoherent motion provides the major contribution to the average longitudinal heat flux at the jet centreline whereas the coherent motion becomes more important for longitudinal heat flux as the distance from the centreline increases.

There are similarities and differences between the present flow topology shown schematically in figure 7 and the topologies that have been proposed for the mixing layer (e.g. Corcos & Sherman 1976) and the near wake of a circular cylinder (Cantwell 1981; Cantwell & Coles 1984). For the mixing layer, the diverging separatrix connects adjacent structures with spanwise vorticity of the same sign. This is similar to the picture that emerges in the far field of the plane jet, on either side of the centreline. For the wake, the diverging separatrix connects adjacent structures on opposite sides of the centreline with vorticity of opposite sign. Cantwell & Coles (1983) (also Coles 1984 and Hussain 1984) emphasized the importance of the vortex stretching near saddles in the context of turbulence production in free turbulent shear flows. They suggested that the turbulence thus produced is transported to and accumulated in regions near the centres of the spanwise structures. We do not have evidence of the latter although there is a clear indication of significantly different spatial distributions for the contributions from the coherent and random motion. The near equality, observed in the present flow, of contributions to the momentum flux due to the coherent and random motions reflects the comparable amplitudes obtained in the near wake of a cylinder (Cantwell & Coles 1983) for contributions from the periodic motion and the random motion at constant phase.

It is possible that the flow topology suggested here includes both the spanwise roller-like structures (e.g. Oler & Goldschmidt 1981, 1982; Mumford 1982) and structures aligned in the direction of the principal axis of strain. The roller-like structures are clearly delineated in figure 7 while the second type of structure could be aligned with the diverging separatrix. Although the present investigation has not provided direct information on these latter structures, it seems plausible by analogy with Hussain's (1984) suggestion for the mixing layer, the braid connecting adjacent structures is not a continuous sheet but consists of slender counter-rotating vortices aligned, on average, with the diverging separatrix. If these counter-rotating vortices are identified with the double-roller eddies (Mumford 1982), the topology of figure 7 implies an intimate connection between the double-roller eddies and the spanwise roller eddies arranged in a Kármán-like vortex street. It should be emphasized however that the two-dimensional representation of figure 7 is only an oversimplified cut through a motion that is in reality three-dimensional and in which strong interactions may occur between neighbouring organized structures.

Large instantaneous temperature and velocity gradients occur at the temperature front, so that the region near the diverging separatrix is also associated with high turbulent-energy dissipation and temperature dissipation. Although the likely interaction between large- and small-scale structures has been recognized for some

time, it would be profitable, in the future, to assess the concept of local isotropy within the framework of a highly spatially organized small-scale motion.

We are grateful for the contributions by Dr S. Rajagopalan in the earlier stages of this work and Mr D. Bissett for later contributions. The support of the Australian Research Grants Scheme is appreciated.

REFERENCES

ANTONIA, R. A., BROWNE, L. W. B., RAJAGOPALAN, S. & CHAMBERS, A. J. 1983 *J. Fluid Mech.* **134**, 49.

ANTONIA, R. A., CHAMBERS, A. J., BROWNE, L. W. B. & RAJAGOPALAN, S. 1984 in *Turbulence and Chaotic Phenomena in Fluids* (ed. T. Tatsumi) p. 529. North-Holland.

ANTONIA, R. A., RAJAGOPALAN, S., SUBRAMANIAN, C. S. & CHAMBERS, A. J. 1982 *J. Fluid Mech.* **121**, 123.

BENDAT, J. S. & PIERSOL, A. G. 1966 *Measurement and Analysis of Random Data.* Wiley.

BLACKWELDER, R. F. & KAPLAN, R. E. 1976 *J. Fluid Mech.* **76**, 89.

CANTWELL, B. J. 1981 *Ann. Rev. Fluid Mech.* **13**, 457.

CANTWELL, B. & COLES, D. 1983 *J. Fluid Mech.* **136**, 321.

CERVANTES DE GORTARI, J. & GOLDSCHMIDT, V. W. 1981 *Trans. ASME* I: *J. Fluids Engng*, **103**, 119.

CHAMBERS, A. J., ANTONIA, R. A., BROWNE, L. W. B. & RAUPACH, M. R. 1983 *Proc. 4th Symp. on Turbulent Shear Flows, Karlsruhe*, p. 15.17.

CHEN, C.-H. & BLACKWELDER, R. F. 1978 *J. Fluid Mech.* **89**, 1.

COLES, D. 1984 In *Turbulence and Chaotic Phenomena in Fluids* (ed. T. Tatsumi) p. 397. North-Holland.

CORCOS, G. M. & SHERMAN, P. S. 1976 *J. Fluid Mech.* **73**, 241.

GOLDSCHMIDT, V. W., MOALLEMI, M. K. & OLER, J. W. 1983 *Phys. Fluids* **26**, 428.

HUSSAIN, A. K. M. F. 1983 *Phys. Fluids* **26**, 2816.

HUSSAIN, A. K. M. F. 1984 In *Turbulence and Chaotic Phenomena in Fluids* (ed. T. Tatsumi) p. 453. North-Holland.

JENKINS, P. E. & GOLDSCHMIDT, V. W. 1976 *Phys. Fluids* **19**, 613.

MOUM, J. N., KAWALL, J. G. & KEFFER, J. F. 1979 *Phys. Fluids* **22**, 1240.

MUMFORD, J. C. 1982 *J. Fluid Mech.* **118**, 241.

OLER, J. W. & GOLDSCHMIDT, V. W. 1981 *Proc. 3rd Symp. on Turbulent Shear Flows, Davis*, p. 11.1.

OLER, J. W. & GOLDSCHMIDT, V. W. 1982 *J. Fluid Mech.* **123**, 523.

PERRY, A. E., CHONG, M. S. & LIM, T. T. 1982 *J. Fluid Mech.* **116**, 77.

RAJAGOPALAN, S. & ANTONIA, R. A. 1981 *J. Fluid Mech.* **105**, 261.

SUBRAMANIAN, C. S., RAJAGOPALAN, S., ANTONIA, R. A. & CHAMBERS, A. J. 1982 *J. Fluid Mech.* **123**, 335.

THOMAS, A. S. W. & BROWN, G. L. 1977 *Proc. 6th Australasian Hydraulics and Fluid Mechanics Conference, Adelaide*, p. 407.

TOWNSEND, A. A. 1976 *The Structure of Turbulent Shear Flow*, 2nd edn. Cambridge University Press.